Supplement

1 CONTENTS

1. KEY TO SUPPLEMENTARY VIDEOS

Video V1: 2D simulation of VACS in Comsol, centre stream velocity of 2.5 m/s.

Video V2: 3D simulation of VACS in Comsol.

Video V3: 2D simulations of VACS in Comsol at a range of steady centre stream velocities from 0.5 to 2.5 m/s.

Video V4: 2D simulation of Stokes flow in the in same geometry: zero fluid density and zero particle mass. No vortex and no deflection.

Video V5: 2D simulation of fluid heating caused by the microresistor actuator.

Video V6: videos of bead trajectories made using strobe imaging (using VACS device with an 80×180-μm microheater)

Video V7: verification of positive sort events* of beads.

Video V8: verification of positive sort events* of PBMCs.

* Note these are not a real-time video, but a compilation of double-flash strobe images. In each frame, the camera shutter is opened, and the strobe LED flashed twice: first at the time of maximum bubble extent, and second after a verification delay time of 500 μs, when the particle has crossed the sorting junction.

2. SUPPLEMENTARY MATERIALS AND METHODS

2.1 COMPUTATIONAL SIMULATIONS

Sorter simulations were carried out in COMSOL Multiphysics® v. 5.2 (www.comsol.com, COMSOL AB, Stockholm, Sweden) using two additional modules: laminar flow and particle tracing for fluid flow. We simulated the vapour bubble using an inlet with a prescribed velocity pulse. Specifically, we assumed that the push and pull of fluid would follow the rise and collapse of the bubble surface, which we modelled as a function of time following: $d(t) = h_b \exp\left[-\left(\frac{t-t_b}{\Delta t_b}\right)^4\right]$, where h_b is the bubble height, t_b is the time when the bubble is at its peak, and Δt_b is roughly half the bubble lifetime. The derivative of this function is then the velocity of the fluid at the inlet.

The sorter inlet channel was set to a length of 2 mm to give a large upstream inertial resistance, while all inlets and outlets have backflow suppression turned off. The pressure at the inlet was set to achieve a certain central flow velocity, as is required for high speed sorting and integration with the upstream inertial focusser, and the pressure at the outlets was set to zero. Bead motion in the fluid was modelled in an uncoupled way, where they felt a drag force given by the Oseen correction to Stokes flow a function of the velocity of the fluid at the beads centre, the bead diameter was set to 10 µm. The medium was set to water in standard conditions, while the bead density was 1100 kg/m^3. The simulated thermal vapour bubble has a peak displacement of 10 µm at the channel wall and a lifetime (expansion and collapse) of 10 µs.

Early in the project, we feared that cells may be damaged by the thermal vapour bubble. Therefore, we simulated the heating of the medium. The actuator is expected to reach a temperature and pressure close to the critical point of water, which would obviously be damaging for a cell. Previous studies measured values up to around 300°C and 45 bar.[1] A 2D simulation of heat and mass flow in a representative geometry: laminar water flow, glass wall, and actuator periodically heated to 300°C for 10 µs at 10-kHz repeat rate. The centre streamline, at 50-µm separation, experiences a maximum temperature rise of 0.1°C (Figure S0 and Video V4). Therefore, it seems plausible that, although the bubble is hot and violent, the cells are far enough away that their viability is not affected. Below, we confirm cell viability experimentally on PBMCs.

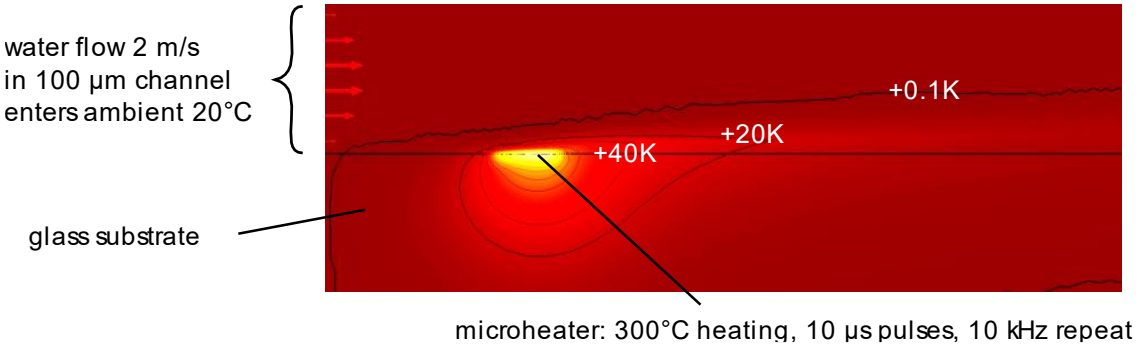

Figure S0: 2D simulation of heating caused by the actuator: the centre-stream reaches a temperature rise of 0.1 K after many cycles at a rate of 10 kHz

2.2 MICROFABRICATION METHODS

Sorter chips are fabricated using standard microfabrication techniques in an ISO 6 cleanroom. Thin film electronic features are deposited and etched on the surface of the glass substrate. Microchannels are moulded in polydimethylsiloxane (PDMS), which is subsequently aligned and bonded to the substrate.

Figure S1 shows an overview of the main process steps. First, a glass substrate (Borofloat BF33) is cleaned using Acetone and IPA spray, then dried using a nitrogen gun and 60°C oven. The substrate is loaded into a MiniLab sputterer (S060M, Moorfield Nanotechnology Ltd., Knutsford, UK) and a layer of titanium followed by a layer of gold are deposited with the DC and RF magnetrons respectively. Various thicknesses were used for experiments: the final design used 170 nm of titanium, followed by 350 nm of gold. The titanium target is first cleaned to remove any native oxide by sputtering for 30 minutes onto a dummy wafer. The substrate is then spin coated (EMS 6000, Electronic Micro Systems Ltd., Salisbury, UK) using Microposit S1818 photoresist (A-Gas Electronic Materials Ltd., Rugby, UK), UV exposed with the tracks mask (EVG 620, EV Group, St. Florian am Inn, Austria) and developed. The gold film is completely etched (Gold etchant, WVR International Ltd., Leicester, UK) and the photoresist stripped. The above process steps are repeated using the resistor mask followed by wet titanium etch (Titanium etchant, A-Gas Electronic Materials Ltd., Rugby, UK). The photoresist is stripped and the final micro heater resistance measured using a set of needle probes (Semi probe MA8005) and a digital multi-meter. The resistance uniformity across a wafer is usually better than 10%. An additional 80-nm silicon dioxide passivation layer was sputtered on top of the wafer using the RF magnetron, and a lift-off mask to expose the electrical contacts.

To fabricate a mould master for the PDMS, SU-8 photoresist (SU-8 3035, Microchem) was spin-coated onto a 100-mm silicon wafer at thickness of 36 µm following the parameters outlined by the manufacturer. Once processed, the wafer was hard baked at 150°C for 3 minutes. The wafer was then silanised by vacuum-depositing (triedecafluoro-1,1,2,2,-tetrahydrooctyl)silane (PFOTCS) to give an non-stick surface modification.

PDMS (Sylgard 184 silicone elastomer, Dow Corning Corporation, Midland, USA) was prepared using the using the standard 10:1 base-to-crosslinker ratio. These were mixed thoroughly and then degassed for 1 hour. The PDMS was then poured over the SU-8 master in a 135 mm petri dish to give a PDMS thickness of 2 mm. The dish was covered and then left to set at room temperature for 2 days. The cold setting of PDMS prevented contraction relative to the thin-film electronic features. Once the PDMS is cured, it was cut out of the petri dish, cut into the component chips, and fluidic ports created using a hole-coring tool mounted in a custom fixture. To bond the glass chip and PDMS microfluidics layer, they were both subjected to O_2 plasma at 350 mT and 20 W power for 30 seconds in a reactive ion etcher (RIE80-GA, JLS Designs Ltd, Unit 4, Camelot Court, Somerton Business Park, Bancombe Road, Somerton, Somerset TA11 6SB). The glass chip and PDMS fluidics were then aligned using a custom fixture which held the surfaces to be bonded roughly 100 µm apart under a microscope. Once aligned, the upper part of the fixture could be pressed down to initiate the plasma bond.

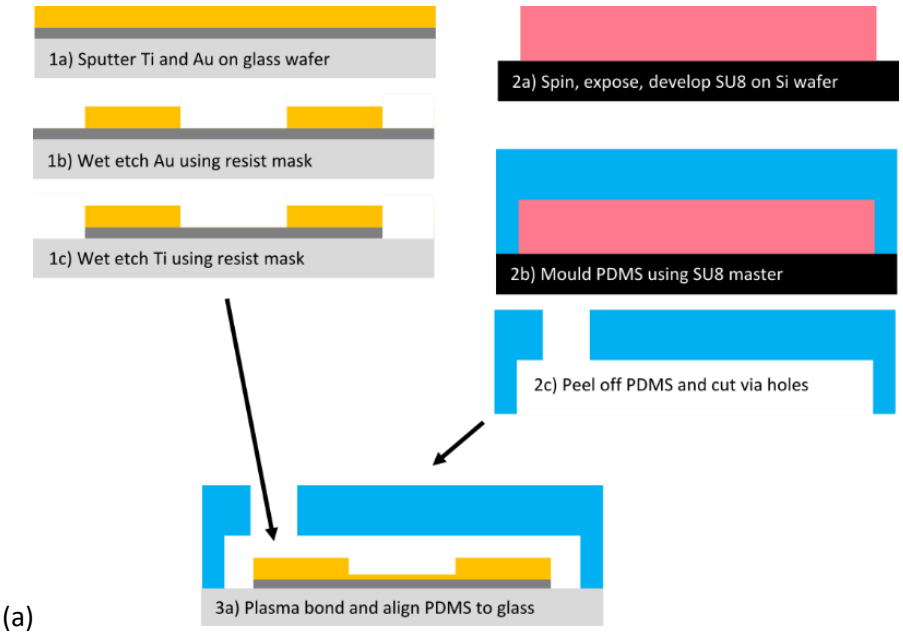

(a)

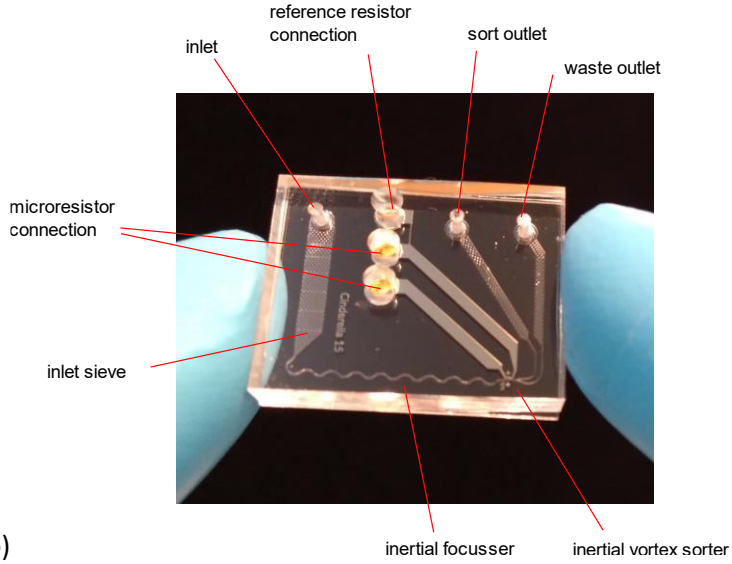

(b)

Figure S1: (a) overview of the main process steps, as described above; (b) complete sorter chip, containing VACS device (bottom right), inertial focusser, fluidic connections, electrical connections and on-chip sieve.

2.3 PULSED LASER ACTUATION

A pulsed laser creates a more controllable thermal vapour bubble than an electrical microheater, since it injects energy into an absorbing liquid in a much more predictable way. The laser pulse transfers a definite amount of energy to a bubble, unlike Joule heating from an electrical microheater, where the energy flows into a complicated combination of the substrate, surrounding fluid and vapour bubble during the phase change.

We therefore used a pulsed laser as a development step in studying the inertial vortex sorter, before we achieved working microresistor actuators.

A Q-switched laser was used to provide intense laser pulses of 30 µJ at wavelength 532 nm. In order to absorb these pulses in a short path length (~ 1 µm) relative to the liquid channel height, an

aqueous solution was made of the dye Allura Red (CAS Number 25956-17-6, catalog number 458848, Sigma Aldrich, Merck KGaA, Darmstadt, Germany) at a concentration of 33.5 g/L, to which 10-µm polystyrene beads were added (catalog number PS-R-10.0, Microparticles GmbH, Volmerstr. 9A, D-12489 Berlin, Germany). When this laser source was focused on the sorter channel, each pulse resulted in a hemispherical bubble of approximately 100-µm diameter.

The laser set-up is illustrated in Figure S2 and described as follows. The Q-switched Nd:YVO_4 laser (Spectra physics, HIPPO), produces 10-ns pulses with a second harmonic of 532 nm. The repetition rate is lowered by the activation of the first pulse suppression (FPS) routine, using the internal pulse trigger with external gate control, pin 17. The repetition rate was 15 kHz (minimum for this type of laser), suppress time about 600 µs, diode current 60%. External gate control was established through a generator with a frequency set close to the inverse suppress time, i.e. 1333 Hz. As the result, a series of pulses of varying intensity was generated (aliasing-like effect).

The laser emission is focused on chip through an infinity-corrected X20 objective lens (Nikon CFI Plan Apo 20x/0.75 WD 1.5 Air UV Objective 0500-0087). Most of the beam was reflected by dichroic mirror DM1 (Thorlabs DMLP550R), the transmitted beam being further attenuated by a coloured glass filter (Filter 1 on Figure S2). Traces of the original emission are detected with a PMT (Hamamatsu). The setup benefits from both reflected light and through-light imaging. The light source is LED with maximum emission at 625 nm (Thorlabs M625L3). 50%/50% non-polarizing beamsplitter (Thorlabs CCM1-BS013/M) is used to separate illumination and reflected light, after passing the beamsplitter cube reflected light is imaged on the left camera. Through imaging is done with infinity-corrected 4X objective lens (Thorlabs TL4X-SAP 4X Super Apochromatic Microscope Objective, 0.2 NA, 17.2 mm WD) and a tube lens which projecting an image on the right camera. Extra dichroic filter DM2 (Comar Optics, 576 IM 125 set at 45˚) is reflecting most of the 532-nm laser beam which is later absorbed by another coloured glass filter (Filter 2). Red LED illumination passing the DM2 filter, then cleaned more with a further coloured glass filter (Filter 3) (Schott Glass, OG590) which absorbs the rest of the 532 nm laser and transparent for wavelengths around 625nm.

The laser pulses of desired intensity are post-selected with an oscilloscope (Pico Technology PicoScope 5000 Series 5442B, PC Based, 4 Channels, 60 MHz) measuring the PMT signal. PicoScope generates an output trigger for camera and for signal generator (Tektronix AFG3022B). Signal generator controls LED activation (through custom-made electronics for fast switching and high current output) by two microsecond-long pulses separated typically by 500 µs. Camera exposure is set long enough to integrate both flashes and finish the frame well before the arrival of next appropriate laser pulse. PMT readings were calibrated with laser power, so that pulses of known energy could be selected, typically 30 µJ for the data presented.

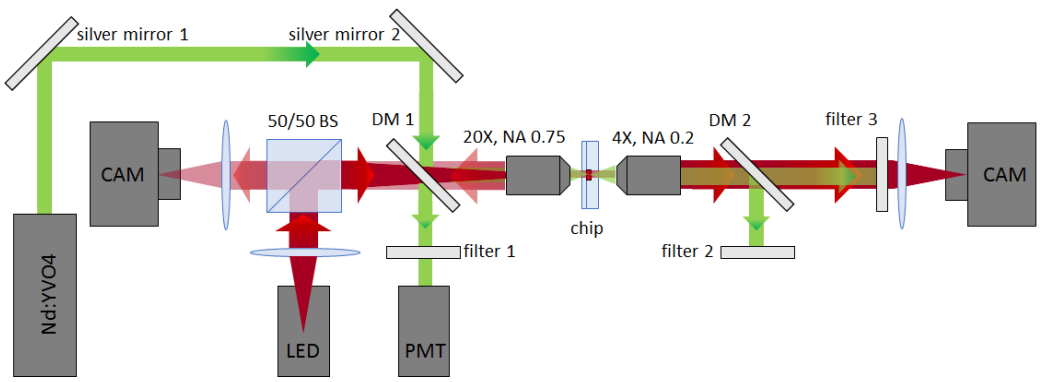

Figure S2: Optical set-up for laser bubble actuation.

2.4 CYTOMETRY OPTICS

Conventional cytometry optics were set up to measure fluorescence, forward and backward scattering of light from a focus in the chip, as shown in Figure S3(a).

A blue-green fibre coupled laser (CW DPSS 488nm, Cobolt) is shaped with auxiliary lenses and a 20X objective lens (Nikon CFI Plan Apo 20x/0.75 WD 1.5 Air UV Objective 0500-0087) to produce a focused Gaussian beam of about 15 µm diameter in waist. The microfluidic sorter chip is positioned so that the focus is in the "measuring position" in the middle of the input channel cross section, just upstream of the sorter. Passing beads or cells scatter light in all directions: back scatter (light scattered at high angles) is collected back through the same 20X objective lens, reflected by a dichroic long-pass mirror DM1 and separated from the original excitation by polarizing beam splitter PBS, which transmits the original laser polarization and reflects the orthogonally scattered light. The back scatter is detected with a photodiode BSC PD. The fluorescence signal is also collected with the same 20X objective lens, and propagates through the first dichroic mirror DM1, then is reflected by the second long-pass dichroic mirror DM2, then detected with a PMT detector (Hamamatsu R647). Forward scattered light is collected with 10X objective lens (OPTEM M Plan APO 10X/0.3 WD 34 28-21-10-000) and reflected by dichroic mirror DM3. A darkfield stop DS is used to absorb direct laser beam so that only the light scattered by certain angle (approximately 5°) is detected on the photodiode FSC PD. Added to this set-up is both transmission and reflection light imaging with a camera CAM and two LED light sources (LED1 and LED2) on opposite sides of the chip, with an emission maximum at 730 nm (Thorlabs M730L4, 515 mW) so that their light propagates through all long-pass dichroic mirrors. An additional 50%/50% non-polarizing beamsplitter BS (Thorlabs CCM1-BS013/M) is used to separate the light source (LED2) from the reflected image light.

The same architecture can be extended to a parallel system, with an array of laser foci and array detectors for fluorescence, forward scatter and back scatter, as shown in Figure S3(b).

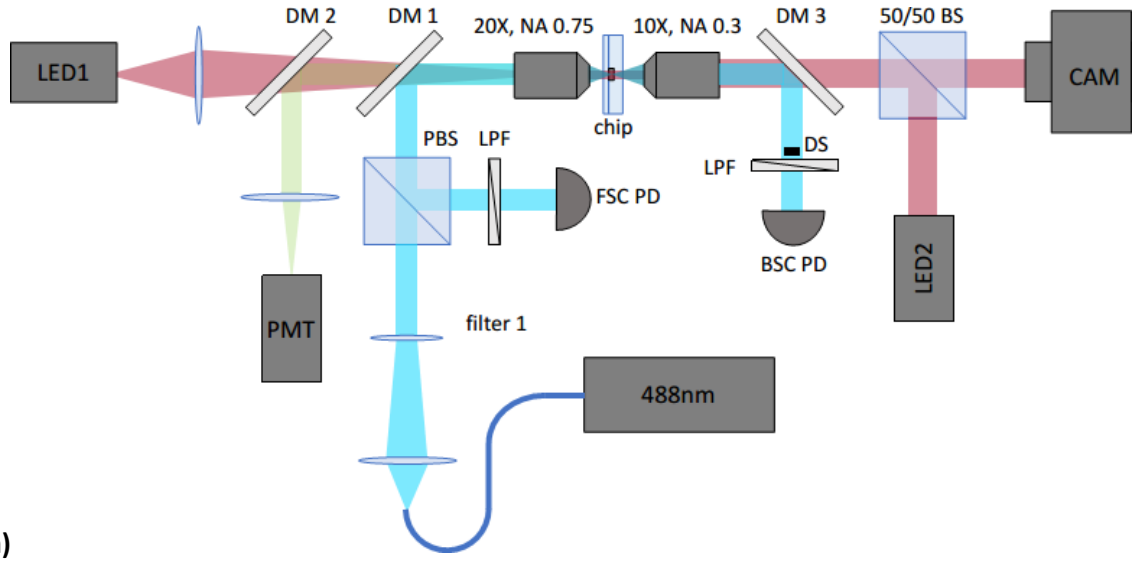

(a)

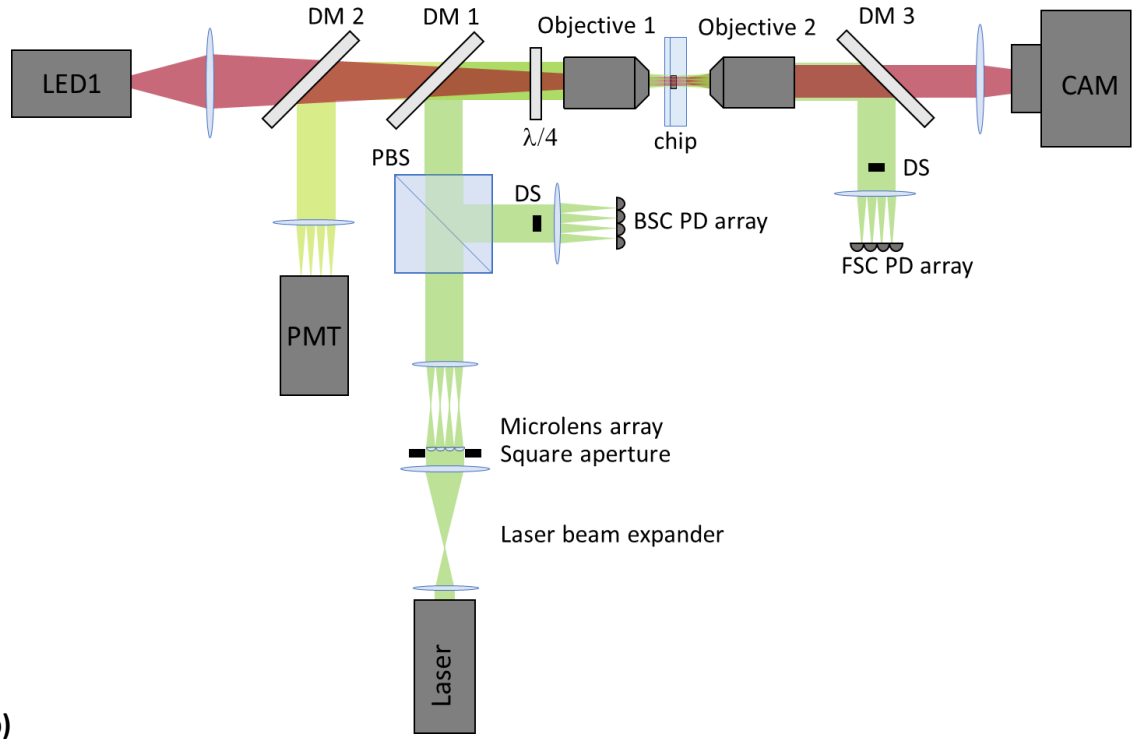

(b)

Figure S3: (a) schematic of cytometry optics for a single sorter. (b) schematic of parallel optical system, for an array of sorters on chip.

2.5 ELECTRONIC CONTROL SYSTEM

An electronic control system was set up to process the optical signals and make real-time decisions of which particles to deflect, sending an output pulse to the actuator.

Briefly, each optical channel (fluorescence, forward and back-scatter) has a dedicated analogue front-end which provides filtering and gain for each optical signal. These are then digitized by 14-bit 8MHz ADCs (THS1408, Texas Instruments, Dallas, Texas, USA) and the signal transferred to the FPGA (DE0-Nano evaluation board by Terasic Inc, Hsinchu City, Taiwan, containing a EP4CE22F17C6N

Cyclone IV chip, Intel Programmable Solutions Group, San Jose, CA 95134, USA) over a parallel interface. The FPGA processes these signals and makes decisions on which cells should be sorted according to simple gating thresholds of peak height, peak area and peak width. For each cell to be sorted, an output pulse is produced according to a delay time after the input pulses. The output signal from the FPGA is connected to transistor switches, so that an electrical pulse is applied to the microheater for a given duration, and a given voltage, set by an adjustable power supply (TTi model EL302P, Aim-TTi Glebe Road, Huntingdon, Cambridgeshire PE29 7DR, UK). The gating thresholds, delay time and actuation pulse duration are parameters set on the FPGA by a PC connection.

The FPGA control system consists of several functions implemented in VHDL blocks and a soft micro-processor. The first VHDL block is the ADC Interface which configures the ADC and converts the data from the parallel interface lines into an integer number to be used in the following block. Next there is a Digital Filtering block which applies a low-pass filter to the incoming data. After this is a Pulse Characterisation block, which characterises the incoming pulse signals by area, width and height. These characteristics of the pulse are then passed to the Event Decision Logic block which decides if this event is a positive particle, based on the thresholds of peak height, area and width. The events are put in a queue so that three intervals can be calculated: the time since the last event, the time until the next event, and the time since the last positive event. These intervals are used to exclude coincidence events (where two particles are within the sort envelope) and to set a minimum repeat actuation time.

When a sort decision is made, then the timing of the detected signals is passed to the Pulse Timing block which waits a for the programmed delay time before switching on the microheater drive signal for the required duration.

The soft micro-processor deals with communication over RS485, this allows configuration settings to be downloaded onto the FPGA and data about the detected events to be uploaded to the host computer.

A schematic of the electronic control system is included in Figure S4.

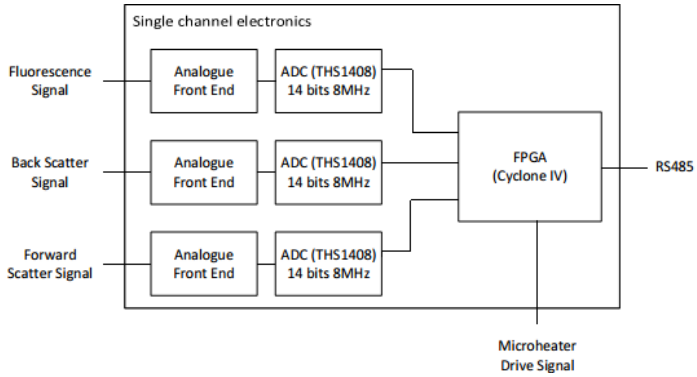

(a)

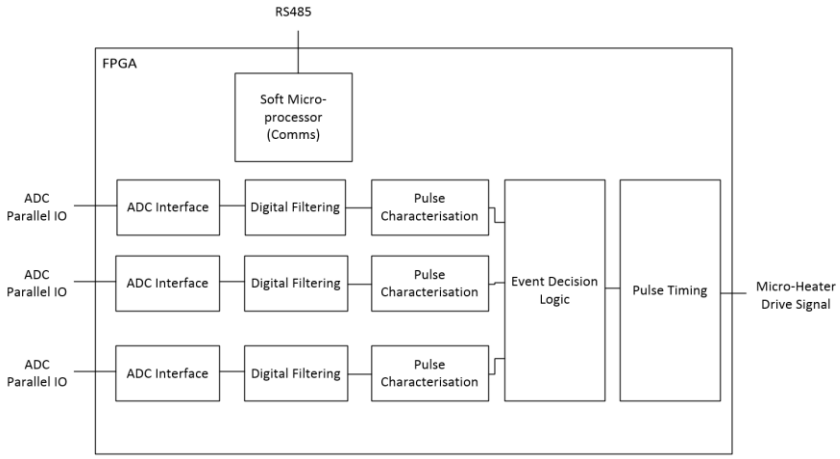

(b)

Figure S4: Schematic of control system described above showing (a) electronics and (b) digital control blocks

2.6 Strobe Imaging and Automated Image Analysis

The optical set-up above was also used for strobe imaging, to collect data from a sample of sort events, adjust the delay time between particle measurement and microheater actuation, and verify the sort efficiency.

Two additional outputs of the FGPA were connected to the camera shutter and the transmission LED for strobe illumination. The maximum sampling rate of sort events was 40 Hz. When a sort event was initiated by the FPGA, the shutter was opened, and the LED flashed twice, each time for a duration of 250 ns, to make two images of the deflected particle. The first flash was given at a delay time to coincide with the maximum extent of the thermal vapour bubble, and the second flash was given 500 µs later, when the particle had passed the sort junction, and could be detected in either the sort or waste channel.

Automated image analysis software was set-up to analyse these strobe images, using OpenCV image processing library for Python (opencv-python version 3.4.1.15; https://pypi.org/project/opencv-python/). In each image, the positions of the two particle images were detected.

To set the detection-actuation delay time for sorting, we followed the following procedure. First, the delay time is ramped, and the two images of the deflected particle are located and tracked. Second, the statistics of correct sort events (deflected bead in sort channel) is binned according to the delay time, which reveals a 'sort envelope': a range of delay times at which almost 100% of the desired particles are sorted. Third, the delay time is set to the middle of this sort window.

2.7 BEAD SORTING AND ANALYSIS

The sorter was tested with various particle populations: polystyrene beads and primary peripheral blood mononuclear cells (PBMCs) as described in the main paper, and an immortal cell line. Fluorescent and non-fluorescent populations were mixed in various ratios to be sorted, to simulate selection common or rare phenotypes.

The beads were either mixtures of 10-µm fluorescent and non-fluorescent polystyrene spheres (product codes PS-FluoGreen-10.0 and PS-R-10.0 respectively, Microparticles GmbH), or mixtures of 6-µm fluorescent and non-fluorescent polystyrene spheres (product codes RCP-60-5 Spherotech Inc and PS-R-6.2 Microparticles GmbH). These were suspended in deionised water, with a small amount of Tween 20 surfactant to prevent bead aggregation and approximately 5% PBS (Hyclone, SH30265.01).

The bead suspensions were diluted to densities of 3×10^5/mL and 3×10^6/mL, so that particle processing rates of approximately 1250/s and 12,500/s were achieved respectively, when pumped at flow rates of 250 µL/min.

The suspensions were introduced to the chip at a controlled flow rate by a syringe pump (Aladdin-220, World Precision Instruments, 175 Sarasota Center Blvd. Sarasota, FL 34240). The beads were not actively mixed within the syringe, so they were continuously settling during the experiment. We found that processing a syringe of up to 5 mL per experiment, i.e. up to 10^7 particles, with a run time of around 20 min, was practical without significant concentration changes due to settling. The sorter was gated on fluorescence area by setting a threshold between the fluorescence and non-fluorescence beads, and on forward scatter width and area, by setting ranges to distinguish between beads and debris.

The sort output was collected (including an extensive rinse of the output tubing, with the chip removed) and measured by a Sysmex Partec CyFlow Cube 8 instrument (Sysmex Partec GmbH, Görlitz, Germany) providing both purity and absolute counts. Recovery was measured from absolute count as (events sorted) / (positive beads counted × total volume output / volume counted).

2.8 IMMORTAL CELL LINE PREPARATION, SORTING AND ANALYSIS

Jurkat cells were prepared, stained and sorted with our devices, with qualitatively similar results to the results with beads and PBMCs. However, since these are of less relevance to cell therapy, we only include one representative result in Supplement 3.7.

Jurkat cells (Sigma, 88042803 – Jurkat E6.1 Cell Line human) were cultured in a T75 flask (Sigma, F7552-1CS) in RPMI medium (Life Technologies, 11875093) supplemented with 100X Penicillin (10,000 Units/mL)/Streptomycin solution (10,000 µg/mL) (Life Technologies,15140122) and 10 % Fetal Bovine Serum (FSB) (Life Technologies, 10500064). Cells were used for experimentation once they had reached a viability of > 90 %.

Jurkat cells were fluorescently stained as follows. The culture was transferred to a 50-mL centrifuge tube and centrifuged at 1500 x g for 2 min. The supernatant was discarded and the pellet resuspended in 1-mL phosphate buffered saline (PBS) solution (Hyclone, SH30265.01). Cells were counted using a haemocytometer and 9×10^6 cells were added to a 15 mL centrifuge tube containing 1 mL of prewarmed PBS and 5 µM CFDA SE cell tracer (Life Technologies, V12883). The tube was inverted several times, protected from light with the cap loose and placed in a humidified atmosphere at 37°C with 5% carbon dioxide for 15 min. The cells were then centrifuged at 1500 x g for 2 min, the supernatant discarded and resuspended in 10 mL HBSS (Sigma, H6648-500ML). This step was repeated two more times and the cells finally resuspended in 1mL of HBSS, protected from light with the cap loose and returned to a humidified atmosphere at 37 °C with 5% carbon dioxide for 30 min.

A mixture of fluorescent and non-fluorescent Jurkat cells was prepared as follows. Unstained Jurkat cells were prepared to a concentration of 3×10^5 cells/mL in 10 mL-HBSS and mixed with stained cells at a final concentration of 3×10^5 cells/mL forming a 1:1 ratio. The 10-mL HBSS cell solution contained 1% FBS (Life Technologies, 10500064), 5mM MgCl (Sigma, M1028-100ML) and 1000 µg DNase (Sigma-Aldrich, D4513-1VL) were added to the cell mixture and the mixture then passed through a 40 µm cell strainer (Corning, 431750). The cells were then processed through the cell sorter.

The Jurkat cells were introduced to the chip by the syringe pump at a flow rate of 275 µL/min, so that the average cell processing rate was 1375/s. As above, the sorter was gated on fluorescence and the sort output was collected and analysed in comparison with the input suspension.

2.9 PBMC PREPARATION, SORTING, COUNTING, FLOW CYTOMETRY AND VIABILITY ANALYSIS

The study was conducted in accordance with Good Clinical Practice and the Declaration of Helsinki 2013, and local regulations. The protocol was approved by the local ethics committee (07/Q0108/3) National Research Ethics Service Cambridgeshire 2 Research Ethics Committee and all study subjects provided written informed consent (n=7, age range 29-64, 3 female).

Human peripheral blood mononuclear cells (PBMC) were isolated from heparinized venous blood (BD Vacutainer® lithium heparin tubes) by density gradient centrifugation. Briefly, 30 mL of blood was layered over 15 mL Ficoll (GE Healthcare) in Accuspin tubes (Sigma) and centrifuged at 800 g for 20 mins (slow acceleration, low brake). The isolated PBMC layer was aspirated and washed twice with PBS prior to being passed through a 40-µm cell strainer. Cells were counted on a Beckman Coulter Z2 counter at a 1 in 100 dilution, measuring particles between 6 and 20 µm in size. All measurements were repeated twice or further until an approximation of the coefficient of variation (CV) was <10%.

PBMC were stained with CD3-BB515, CD19-PECy7 and CD14-APC; CD19-BB515, CD3-PECy7 and CD14-APC (all BD Biosciences) or LIVE/DEAD Fixable Near-InfraRed (ThermoFisher Scientific).

Antibodies used: CD3 BB515 (PN 564560; Lot 7227847; Clone SK7), CD19 BB515 (PN 564456; Lot 8025983; Clone HIB19), CD19 PE-Cy7 (PN 560728; Lot 7215753; Clone HIB19), CD3 PE-Cy7 (PN 563423; Lot 7208958; UCHT1), CD14 APC (PN 555399 & 561708; Lot 7116537 & 7195873; M5E2 (both))

PBMC suspensions were pumped through the sorter at 220 µL/min, resulting in cell processing rates of around 4 – 10×10^3 cells/s.

PBMC sorting was gated using the following process. First, a histogram of forward scatter width was plotted, and upper and lower thresholds selected to remove doublets and sub-cellular particles. Second, a scatter graph of forward scatter area versus fluorescence area was plotted, and upper and lower thresholds selected. This process allowed reasonably pure selection of the lymphocytes labelled by the single fluorescent marker. An example of the process is shown below in Figure S11.

Standard commercial instruments were used to measure the performance of the sorter, according to the following scheme: pre-sort and sort output cell densities was measured with a Z2 Coulter counter (Beckman Coulter, 5350 Lakeview Parkway S Drive, Indianapolis, IN 46268, USA), and pre-sort positive fraction and sort output purity were measured with a FACSCanto II flow cytometer (BD Biosciences, 2350 Qume Drive San Jose, CA, USA).

Recovery was calculated from the above data as ndp/Nf, where n and N are the cell densities in the sort and pre-sort respectively, d = 0.4 is the proportion of the volumetric flow that goes into the sort output, f is the pre-sort positive proportion, and p is the sort purity. Although it is also possible to calculate recovery from the positive fraction in the waste, this would be subject to greater errors due to sticking of sub-cellular particles and debris in the tubing, which lead to counting errors.

Viability was measured immediately less than 2 hours after sorting, using the LIVE/DEAD Fixable Near-InfraRed stain and the gating strategy shown in Figure S5.

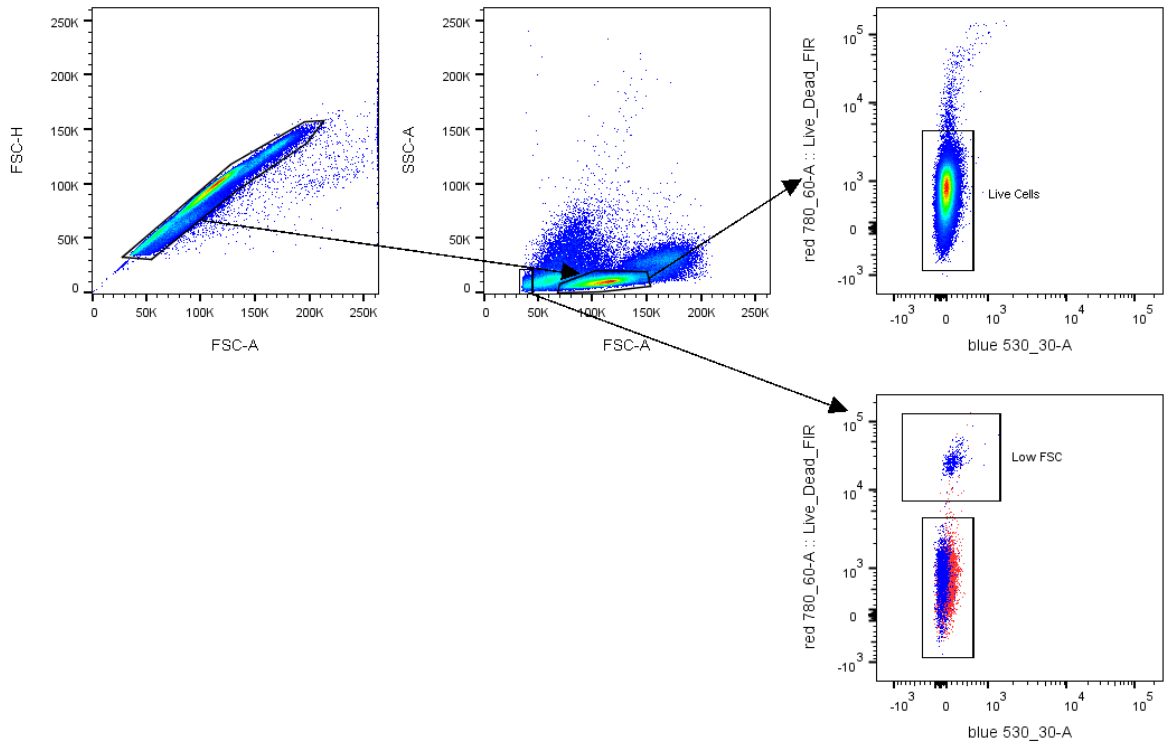

Figure S5: Gating strategy used to determine cell viability pre- and post-sort. FSC-H vs FSC-A were used to identify single cells (defined as the population where FSC-H is approximately equal to FSC-A). Lymphocytes were then gated on low SSC-A/mid FSC-A, as in Figure 3, live cells are those with low quantities of LIVE/DEAD dye and low FSC particles are shown here backgated onto the live cells to demonstrate the distinction between live and dead cells.

2.10 INERTIAL FOCUSSING AND PARTICLE VELOCITY MEASUREMENTS

We iterated through several designs of inertial focuser, settling on a design which would focus denser-than-water particles, including 6-µm and 10-µm polystyrene beads (catalog numbers PS-R-6.2 and PS-R-10.0, Microparticles GmbH) and cells, including primary leukocytes (circa 6-8 µm) and Jurkat cells (circa 14 µm), into a single line.

This inertial focuser design was effective at focusing particles in the appropriate size range. Since the focuser is a symmetric serpentine design, it appears to differ slightly in operation from the inertial focusing theory of Di Carlo et al. [2] but is alternatively described by the theory of Zhang et al. [3]. The channel height was 35 +/- 2 µm, the curvature is defined by 15 circular arcs of 98 degrees and radius of 500 µm, of alternating direction, as shown in Figure S6(a). Two channel widths were tested: 90 µm and 70 µm; the latter showing reduced error rates for smaller particles, as described below. A straight section was included in this test design, downstream of the focusser, for microscopic measurement of particle focussing.

The inertial focussers were tested quantitatively on a mixture of 6-µm and 10-µm polystyrene beads (catalog numbers PS-R-6.2 and PS-R-10.0, Microparticles GmbH) suspended in DI water, using our strobe microscopy set-up and automated image analysis to detect the bead position, size and speed, in the straight section of the test channel, downstream of the inertial focusser. The bead suspension was pumped into the test chip at a rate of 250 µL/min. Measurements of focussed bead velocity were used to give a conversion factor between centre-stream velocity and volumetric flow rate for subsequent experiments.

Table S0 shows the full results for both designs; Figure S6(b) and (c) show the results for the 70-µm-width version. Figure S6(b) shows a composite of all the strobe microscopy frames showing tight focussing of 6-µm and 10-µm beads in the centre of the channel. Figure S6(c) shows histograms of deviation of 6-µm and 10-µm beads on the same axis.

To avoid false positives, the beads need to be focussed tightly enough that they do not accidentally go into the sort channel. At the same time, to avoid false negatives, the predicted deflection of 18 µm should be enough to send a focussed bead into the sort channel. Thus the deviation should be smaller than the deflection minus the diameter of the particle. We therefore chose a threshold acceptable deviation of 7.5 µm. As shown on Figure S6(c), for the 70-µm version 99.27% of the 6-µm and 100% of the 10-µm beads are focussed with less than this deviation (with full results in Table S0). Considering that the deviation is in both directions, we would expect the non-perfect focussing to cause a false positive rate of the order of 0.4% for 6-µm beads, but 0% for 10-µm beads in the 70-µm version. The 70-µm version was employed for all sorting performance measurements quoted in the paper.

A further measurement was made in the full sorter chip, of the velocity ratio between the sort envelope position and the downstream 90-µm-wide straight section, pumping the 10-µm bead suspension into the sorter at a rate of 275 µL/min, and measuring particle velocity using the same strobe technique. A composite image of the focussed beads path through the sorter is shown in Fig S6(d). The ratio between the speed in the sort window and the input channel was found to be 89% +/- 5%. These measurements of focussed bead velocity was used to give a conversion factor between spatial units and temporal units for sort mask width in subsequent analysis.

Measurement	90 µm width	70 µm width
Velocity	2.27 +/- 0.12 m/s	2.73 +/-0.05 m/s
Proportion of 10-µm beads with deviation < 7.5 µm	100%	100%
Proportion of 6-µm beads with deviation < 7.5 µm	95.2%	99.3%
Expected false positive rate for 10-µm beads	0%	0%
Expected false positive rate for 6-µm beads	2.4%	0.4%
Number of measurements 6-µm beads	688	1102
Number of measurements 10-µm beads	342	399

Table S0: performance measurements of the inertial focusser in the 90-µm- and 70-µm-width versions.

(a)

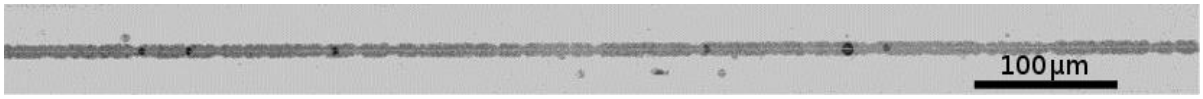

(b)

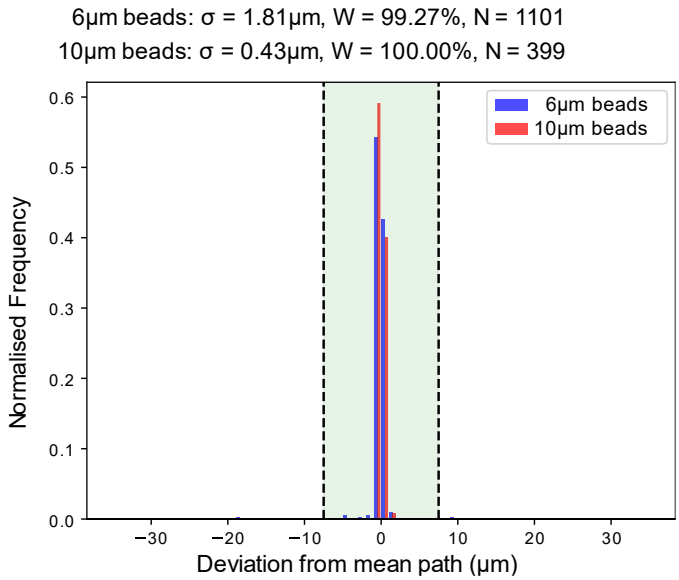

(c)

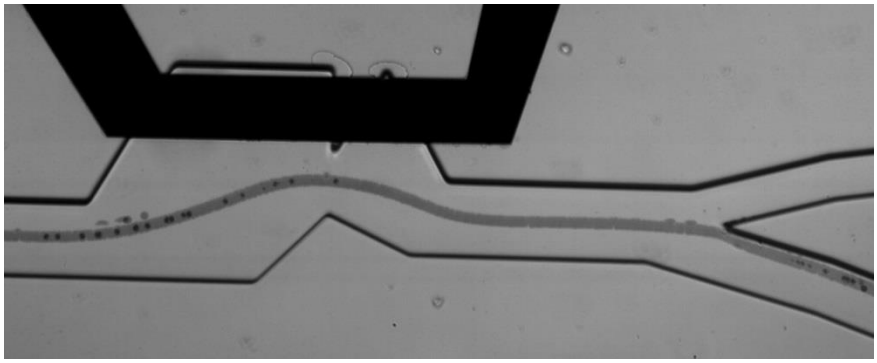

(d)

Figure S6: (a) design of the inertial focusser; (b) composite of many strobe microscopy frames showing tight focussing of 6-µm and 10-µm beads in the centre of the channel; (c) histograms of deviation of 6-µm and 10-µm beads on the same axis, showing respectively 99.3% and 100% are focussed with deviation < 7.5 µm; (d) composite of many strobe microscopy frames of focussed 10-µm beads in the sorter.

2.11 PURITY AND RECOVERY OF A THEORETICAL IDEAL SORTER

An ideal sorter is defined as producing errors due to coincidence events only, i.e. no other sources of false positives or false negatives.

We assume that the arrival time of particles in an ideal sorter is a Poisson process; i.e. the positions of the particles in the stream are uncorrelated. Although this assumption ignores known effects such as clumping of particles, the mutual exclusion of solid particles, and the entrainment of particles by inertial effects, it is still a useful assumption to calculate what an ideal sorter should achieve.

Poisson statistics are used as follows to calculate the purity and recovery, assuming certain properties of the ideal sorter: a sort envelope time t_e, where particle deflection probability is 100% within and 0% outside of this envelope; and a minimum actuation repeat time t_m, for triggering a new sort event.

2.11.1 High-purity mode

In high-purity mode, the ideal sorter rejects all coincidence events. Thus the purity of the ideal sorter output is 100%, but the recovery is reduced by the probability of desired particles being excluded by coincidence events and the minimum repeat time of actuation.

To calculate the recovery, we consider a sequence of events, starting with a positive event which we wish to sort. There may be coincidence events within a time $t_e/2$ preceding or succeeding the start event, which would cause us to reject the positive event: the probability of this occurring is $\mathrm{e}^{-\mathrm{rt_e}}$, where r is the rate of arrival of particles. Then there may be positive events following the start event which are within the minimum repeat time, and therefore would go to waste. The expected number of additional positive events within this time is $\mathrm{frt_m}$ where f is the positive fraction in the pre-sort population. Thus the ideal recovery is $\mathrm{e}^{-\mathrm{rt_e}}/(1 + frt_m)$.

2.11.2 High-recovery mode

In high-recovery mode, the ideal sorter does not reject coincidence events. The only source of impurity is coincidences, and the only loss of recovery is due to the finite minimum repeat actuation time.

Starting with a positive event that we wish to sort, the expected number of coincidence events within the sort envelope is rt_e of which frt_e are positive. Thus the ideal purity is $(1 + frt_e)/(1 + rt_e)$ while the ideal recovery is $(1 + frt_e)/(1 + frt_m)$.

3. SUPPLEMENTARY RESULTS

3.1 SIMULATION OF THE VORTEX SORTER CONCEPT

2D simulations in COMSOL predicted the sort envelopes listed in Table S1, as a function of stream velocity. We also made a 3D version of this simulation which shows qualitatively the same behaviour: animations of both 2D and 3D simulations are in the Supplement V1-V2.

A range of input flow velocities were tested in the simulation. Remarkably, the inertial vortex effect is predicted to work at a wide range of flow speeds (centre velocity from 0.5 to 2.5 ms^{-1}). Throughout this range, the 'sort envelope' is predicted to be approximately constant spatially: a contour of around 20 µm along the flow path gets sorted, while the envelope time varies approximately inversely with the flow rate. Animated results are shown in Supplement V3.

Centre-stream velocity [ms^{-1}]	Sort envelope time [µs]	Sort envelope contour [µm]
0.5	105	53
1.0	27	27
1.5	12	17
2.0	9	18
2.5	8	20

Table S1: simulation of the inertial vortex effect at a range of input flow velocities

3.2 ACTUATION BY PULSED LASER AND UNTRIGGERED PARTICLE DEFLECTION

We set up a version of the vortex sorter in the pulsed laser rig, as described above. We used a dye in the solution to absorb the pulse energy within a depth of around 1 µm. The laser pulse duration was around 10 ns and focus size was around 15 µm: both much smaller than the expansion time and size of the resulting thermal vapour bubble.

10-µm polystyrene beads were focused by the inertial focusing element and carried at a centre-stream velocity of 2.5 ms^{-1} in the sorting region. Since we had not set up optical analysis or triggering of the laser pulses in this experiment, the laser was simply allowed to fire 30 µJ pulses at a regular rate of 1 kHz, with each pulse creating a thermal vapour bubble. At each laser pulse, beads were present at random locations; we thus obtained random sampling of the deflection as a function of the bead's location in the flow. Camera frames were captured for a subset of the laser pulses. In each frame, the LED illumination was pulsed twice: once triggered by the laser pulse, and a second time with a delay of 500 µs. The field-of-view was set up to capture the entire sorter geometry, including the input channel at a distance of 1.5 mm upstream.

It was quickly apparent that particles were deflected only if the particle was in the region of the sharp edge at the time of actuation. Figure S7(a) shows an example: the first image of the particle is in the 'firing zone' (confirmed by the lack of an upstream particle image); the second image of the particle is in the sort channel. After examining many frames, it was apparent that all other particles went down the waste channel. Figure S7(b) shows a superposition of particle positions in frames, chosen manually, where the particle's first image was unambiguously in or near the firing zone. The particle positions are marked on the image according to whether the second image of each was in the sort or waste channel. There is a clear sort envelope, where all the particles were sorted, and outside of which, no particles were sorted.

The Q-switched laser-actuated rig has various disadvantages with regard to building a practical sorter instrument: it requires a dye to absorb the laser energy, and is based on a laser that is

designed to operate repeatedly at far higher rates than we wish to sort. It would also be complicated and costly to use such a laser to operate multiplexed sorters on a chip. We therefore chose to concentrate on electrical microheater actuators to build a practical cell sorter.

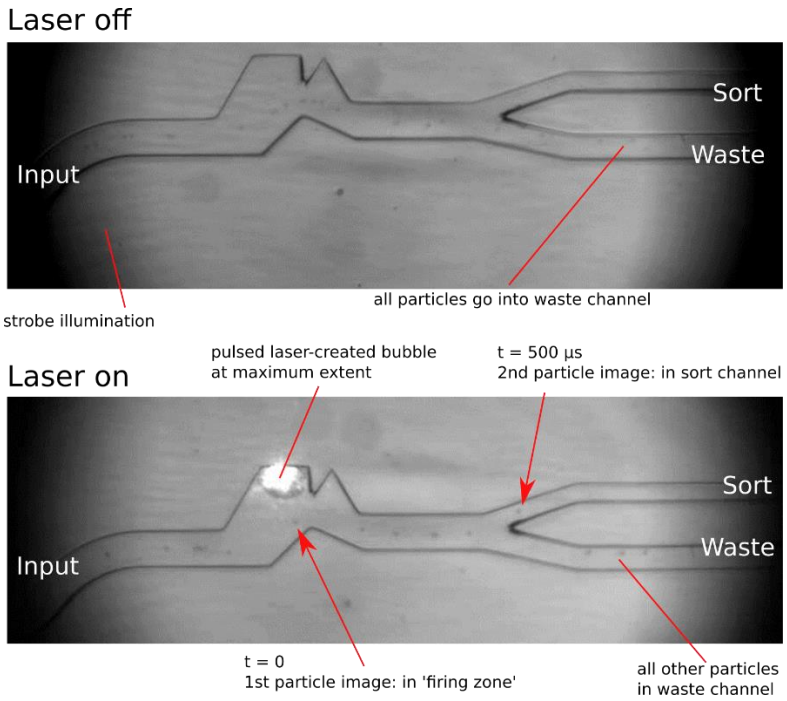

(a)

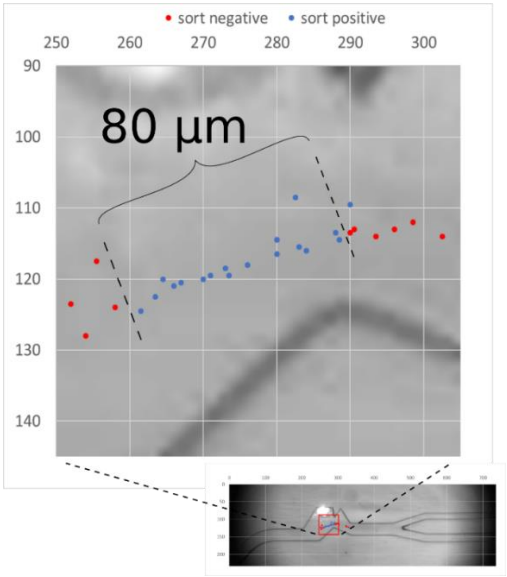

(b)

Figure S7: pulsed laser bubble creation and deflection of beads. (a) Double strobe image of a 10 µm bead deflected by a Q-switched laser-generated bubble. (b) Superposition of particle positions in a set of manually-chosen frames, sampling particle position at the 'firing zone'. Positions are colour-coded according to whether the particle arrived in the sort or waste channels. A clear 'sort window' of approximately 80 µm contour length is apparent.

3.3 DESIGN AND TESTING OF ELECTRICAL MICROHEATER ACTUATORS

Microresistors on a glass substrate were built as described above, and connected to a laboratory signal generator and strobe microscopy set-up. Figure S8 shows strobe illumination of expanding and collapsing bubbles, firstly in bulk liquid, and secondly surrounded by the microchannel. Figure S8(a) shows strobe images of a bubble in free liquid: an energy dissipation of only 1.8 µJ creates a bubble of volume around 0.3 nL, which peaks around 3 µs after nucleation (30-V pulse amplitude, 0.3-µs pulse duration, 100×40-µm resistor area, 84 nm resistor thickness). However, when surrounded by our sorter device, a much larger energy dissipation is required to create a comparable bubble volume. Figure S8(b) shows strobe images of a bubble in the channel: an energy dissipation of 25 µJ creates a bubble of volume around 0.1 nL, which also peaks around 3 µs after nucleation (30 V pulse amplitude, 3 µs pulse duration, 80×180 µm resistor area, 92 nm resistor thickness, in a flow of deionized water at 250 µL/min). This is because the bubble expansion encounters a much greater resistance within the channel compared to the free liquid: instead of the fluid displacement occurring in all directions, the bubble is forced to accelerate the liquid along one-dimension columns within the microchannels.

Confirming what is known in the bubblejet literature[1], we found that for a given voltage, increasing the pulse duration only increases bubble size up to a certain critical time, at which homogeneous nucleation occurs across the heater surface: beyond this point, the liquid is thermally isolated from the heater. The homogeneous nucleation point can be seen in Figure S8 as the first frame in both image sequences (a and b).

Table S2 shows a set of electrical pulse amplitudes and durations, the resulting bubble size and lifetime, and the energy dissipated at the heater by Joule heating, for a 100×40-µm microresistor in free liquid. In each case, we have set the duration just long enough to see the homogeneous nucleation across the heater surface. Volumes are estimated as the bubble width cubed, since we do not have depth information. Lower voltages allow longer heating times, which allow greater energy dissipation and larger bubbles: these all confirm results from the bubblejet literature [1]. The same trend was observed for a heater placed within the channel, but it was unfortunately not practical to repeat the measurements within the flow channel, because the appearance of the bubble was also much less regular.

We found that lifetime of the heater depended on actuation rate and fluid medium. Maximum sustained actuation rate for this construction of microresistor was 12 kHz, for 80×180-µm microresistors with a 30-V, 3-µs pulse, in the channel with a flow of PBS at 250 µL/min. However, we limited the sustained actuation rates to around 1 kHz for our bead separation and cell separation experiments below, to allow processing of batches of ~10 million cells while achieving a high recovery for rare positive populations. In these conditions, microresistors survived $>2\times10^6$ cycles before any noticeable drop in sorting performance. There are well-known methods of extending the microresistor lifetime used in the inkjet industry: modulating the pulse durations so that a following pulse has lower energy than a preceding pulse (reflecting the cooling timescale of the microresistor), as well as the inclusion of several additional thin film passivation layers on top of the microresistor. However, we have not yet implemented these technical improvements. However, we note that sustained actuation rates of >15 kHz have been achieved more than 20 years ago with commercial thermal inkjet printer technologies[4], and now reach around 100 kHz for billions of cycles.

3.4 STROBE EVALUATION AND MEASUREMENT OF SORT ENVELOPE

The sort envelope is measured by double-flash strobe imaging. Sort events are sampled at maximum rate of 40 Hz. In each frame, the strobe LED is flashed twice: first at the maximum bubble extent (firing delay time, plus microheater pulse time, plus bubble growth time) and second after a verification delay time of 500 µs, when the particle has crossed the sorting junction.

As shown in Figure S8(c), a minimum resistor size of 80×120 µm was required to sort particles, but reliable high-efficiency sorting required resistor size of at least 80×180 µm. Representative images and sort envelopes are plotted for the 80×120, 80×180 and 100×240-µm microheaters. Each sort envelope contains statistics of at least 2000 beads. A composite image shows that position within the firing zone and position in the sort channel are correlated; indeed there are apparently two distinct sets of beads in the sorted stream. These seem to correspond to the two inertial foci overlaid in the plane of the chip: beads in each focus seem to experience the vortex slightly differently.

Ideally, the probability of deflection is 100% within and 0% outside the sort envelope. False positive and false negative error rates can be estimated from the observed statistics: for the 80×180 µm microresistor event statistics, all 1702 particles tracked outside the envelope entered the waste and zero entered the sort channel. However, in the central 26 µm of the sort envelope, 398 particles were tracked: all these particles entered the sort channel and zero entered the waste. Therefore we estimate upper bounds on false positive rate of <0.06% and false negative rate of <0.25% for the core device's deflection ability.

Pulse voltage [V]	Pulse duration [µs]	Energy dissipation [J]	Bubble lifetime [µs]	Peak time after nucleation [µs]	Bubble width at maximum [µm]	Estimated volume [nL]
16	4.3	7.32E-06	11	3	86.9	0.66
18	2.7	5.82E-06	10	3	85.1	0.61
20	2.0	5.32E-06	10	3	82.9	0.57
25	0.7	3.12E-06	9	3	76.0	0.44
30	0.3	1.79E-06	8	3	66.9	0.30

Table S2: bubble size, lifetime and heat energy, as a function of electrical pulse voltage and duration. Volume is estimated as bubble width cubed.

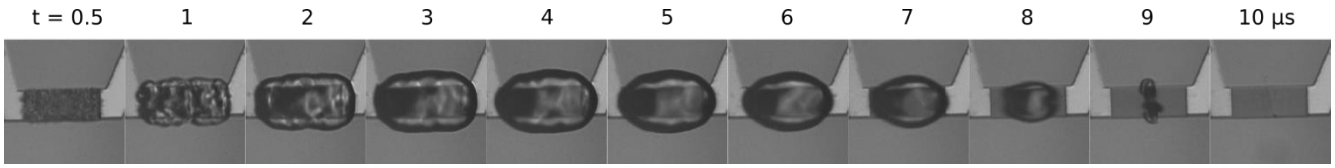

(a)

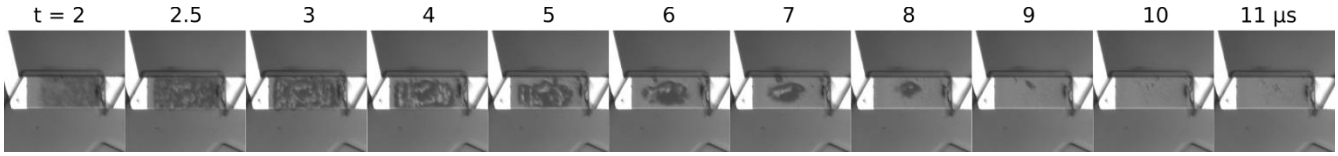

(b)

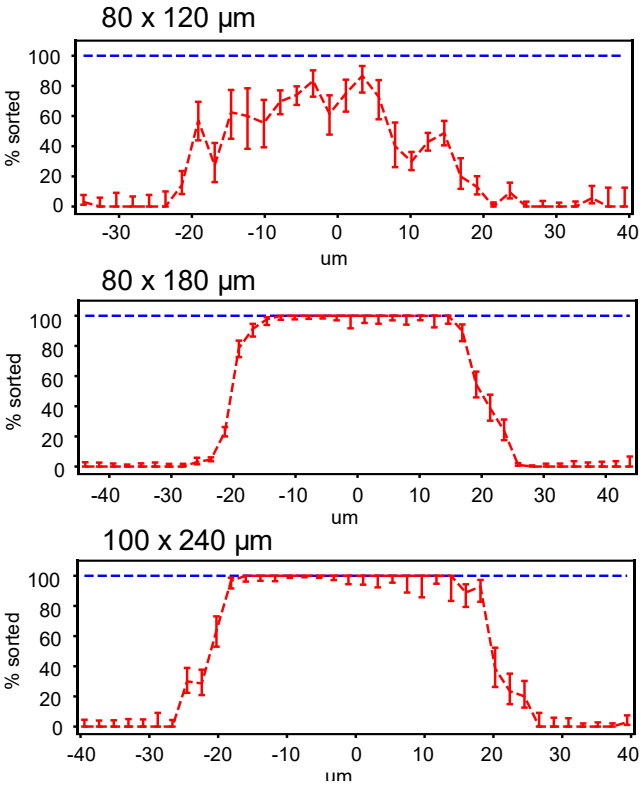

(c)

Figure S8: strobe images of expanding and collapsing bubbles on an electrical microresistor actuator, in the free liquid (a) and in the sorter microchannel (b). For a comparable bubble volume, a much larger energy pulse of 25 µJ is required in the channel, compared to 1.8 µJ in the free liquid. (c) Histograms of sort events showing sort envelopes for various sizes of microresistor actuators: efficient sorting is achieved with resistors around 80×180 µm and greater.

3.5 PARTICLE DEFLECTION WITH ELECTRICAL MICROHEATER ACTUATION, OPTICAL ANALYSIS AND IMAGING

Tables S3 and S4 provide analysis of the sort envelope and sort efficiency measured by strobe analysis of sort events. The data shows no loss of efficiency (defined as proportion of sort-positive events that are correctly sorted) up to 5 kHz, which is the limit of our current real-time signal processing.

Centre-stream velocity [ms^{-1}]	Sort envelope time [µs]	Sort envelope contour [µm]
1.0	70	62
1.5	44	59
2.0	29	52
2.5	23	52

Table S3: experimental results for the inertial vortex sort window at a range of flow rates; thermal vapour bubble actuation is with a 80×180-µm microheater.

Peak sort rate [Hz]	Particles triggered	Particles sorted	Sort efficiency
100	738	737	99.9%
500	789	788	99.9%
1000	903	903	100.0%
2000	970	968	99.8%
3300	791	791	100.0%
5000	1176	1173	99.7%

Table S4: sort efficiency for peak sort rate up to 5 kHz.

3.6 SORTING OF JURKAT CELLS

The sorter was tested on Jurkat cells in high-recovery mode, where a fluorescent subpopulation was created using CFDA-SE staining as described above. A representative example is shown in Figure S9, achieving 95% output purity (starting from an input positive fraction of 64%).

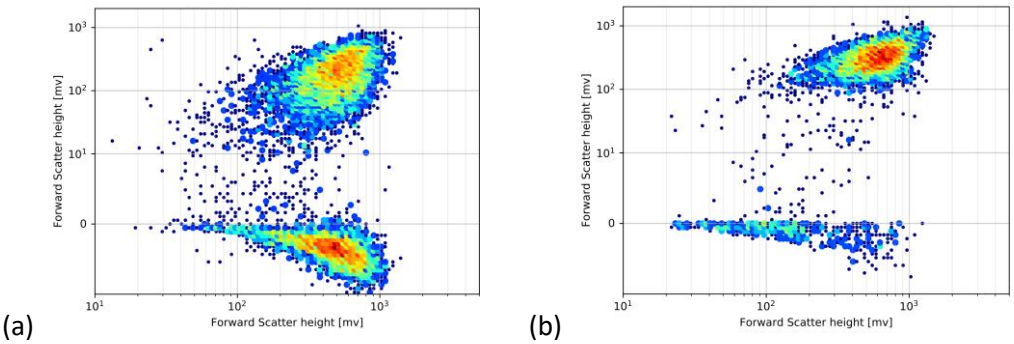

(a) (b)

Figure S9: Representative separation of Jurkat cells, with an arbitrary CFDA-SE-positive fluorescent subpopulation: input positive fraction of 64% (b) and 95% output purity (b).

3.7 SORTING OF PBMCS

The purity and recovery of the PBMC separations are shown below (all high-purity mode). The minimum repeat time was set at 100 µs for the CD19 separation, i.e. 10 kHz peak sort rate, but 1000

µs for the CD3 separation, to limit the sustained sort rate to 1 kHz for the common cell sort, in order to prevent degradation of the heater.

Since, in comparison to beads, PBMC suspensions contained many doublets, sub-lymphocyte particles and debris, the process of gating was more complicated than for beads, as described above. Figure S10 shows an example of the gating process for a B-cell separation.

Figure S10(a) shows forward scatter area against fluorescence area of all particles detected. The populations are not distinct, due to doublets and low-FSC particles. These can be effectively gated out using forward scatter width, as shown in Figure S10(b). The lymphocyte population has a distinct peak, while the low-width tail includes sub-lymphocyte particles and debris, and the high-width tail includes doublets. Having removed these particles, the $CD19^+$ lymphocytes are much more distinct from the $CD19^-$ cells, allowing a B-cell gate defined by forward scatter area and fluorescence area thresholds as shown in Figure S10(c).

Ideal sorter purity and recovery were calculated using the equations above, taking t_e = 23 µs and the relevant minimum repeat time, input rate and pre-sort fraction.

	Input rate [/s]	Pre-sort CD3+ fraction	Output purity	Recovery	Ideal sorter purity	Ideal sorter recovery
Subject 1	5.11E+03	50.40%	88.00%	20%	100%	25%
Subject 2	4.49E+03	84.80%	98.60%	10%	100%	19%
Subject 3	3.10E+03	78.00%	98.70%	16%	100%	27%
Subject 4	5.54E+03	61.10%	97.10%	22%	100%	20%
Subject 5	7.31E+03	63.20%	97.60%	16%	100%	15%
Median	5.11E+03	63.20%	97.60%	16%	100%	20%

Table S5: T-cell repeat sorts.

	Input rate [/s]	Pre-sort CD19+ fraction	Output purity	Recovery	Ideal sorter purity	Ideal sorter recovery
Subject 1	7.67E+03	4.13%	92.40%	35%	100%	81%
Subject 2	7.33E+03	1.16%	79.10%	136%	100%	84%
Subject 3	7.11E+03	1.17%	85.30%	114%	100%	84%
Subject 4	7.68E+03	1.71%	75.60%	68%	100%	83%
Subject 5	8.98E+03	1.35%	82.40%	86%	100%	80%
Subject 6	6.63E+03	1.22%	81.80%	126%	100%	85%
Subject 7	8.28E+03	3.16%	90.90%	29%	100%	81%
Median	7.67E+03	1.35%	82.40%	86%	100%	83%

Table S6: B-cell repeat sorts.

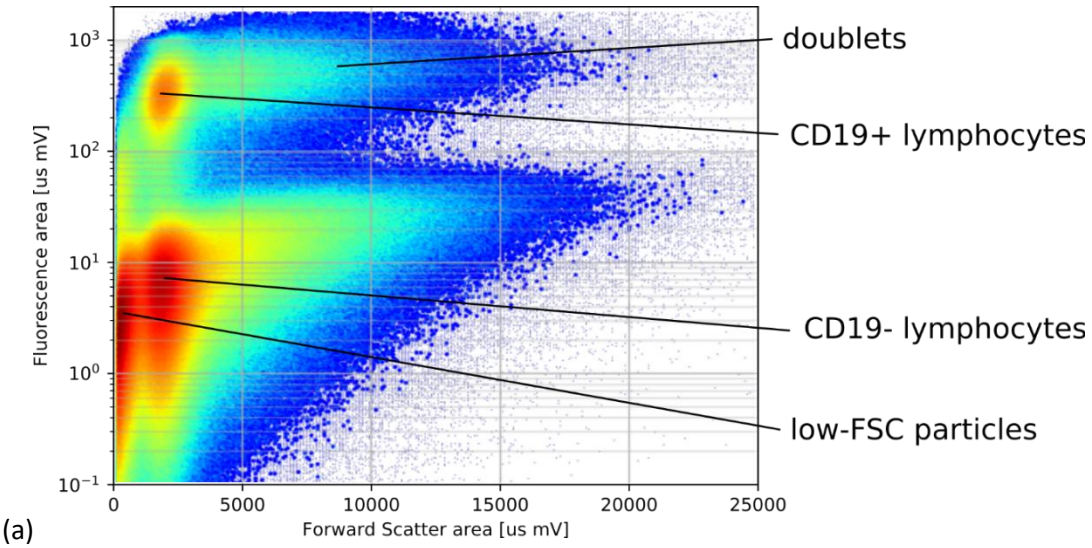

(a)

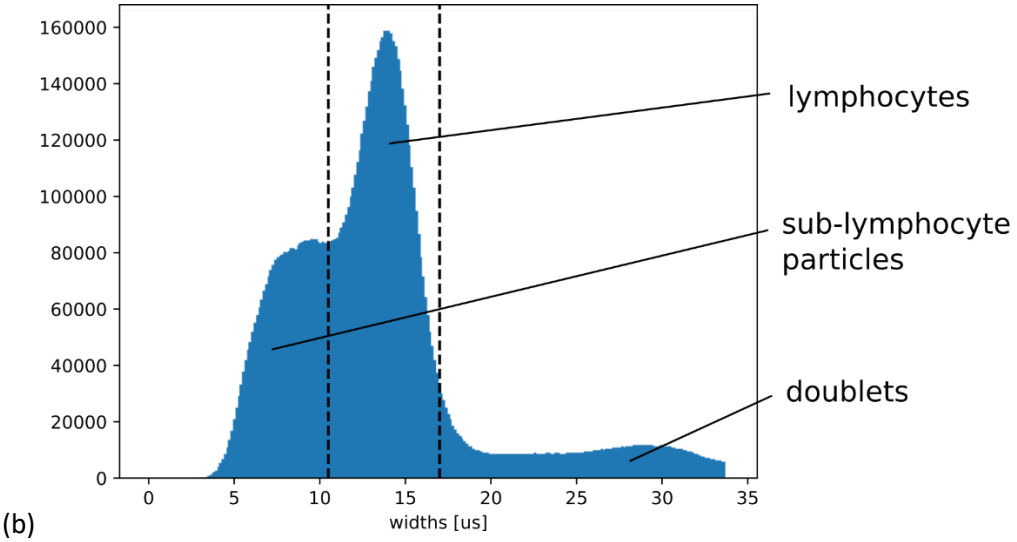

(b)

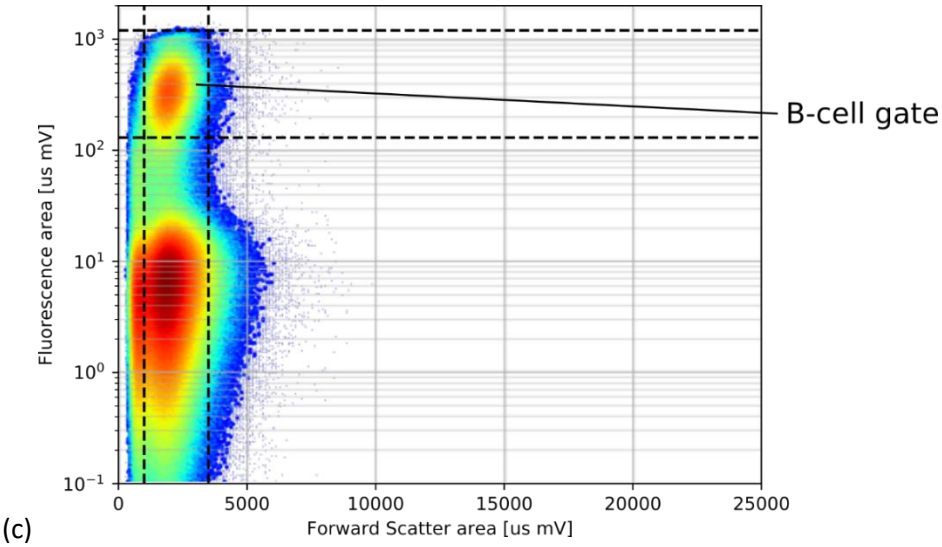

(c)

Figure S10: (a) all detected particles – populations are not distinct due to doublets and low-FSC particles; (b) forward scatter width gate allows removal of sub-lymphocyte particles and doublets; (c) forward scatter area and fluorescence area thresholds allow a B-cell gate.

3.8 VIABILITY OF PBMCS

Viability immediately post-sort was measured on 4 subjects' PBMCs, using the method above. A sample of the unstained PBMCs were sorted randomly, and the sort output compared to the pre-sort control.

	Pre-sort	Sort output
Subject1	99.4	99.5
Subject2	99.5	99.2
Subject3	97.7	99.6
Subject4	99.3	99.8
Mean	99.0	99.5

Table S7: PBMC viability pre- and post-sort.

SUPPLEMENT REFERENCES

1. Hong, Y., Ashgriz, N. & Andrews, J. Experimental Study of Bubble Dynamics on a Micro Heater Induced by Pulse Heating. *J. Heat Transf.* **126,** 259–271 (2004).
2. Di Carlo, D., Irimia, D., Tompkins, R. G. & Toner, M. Continuous inertial focusing, ordering, and separation of particles in microchannels. *Proc. Natl. Acad. Sci. U. S. A.* **104,** 18892–18897 (2007).
3. Zhang, J. *et al.* Inertial particle separation by differential equilibrium positions in a symmetrical serpentine micro-channel. *Sci. Rep.* **4,** 4527 (2014).
4. Beeson, R. Thermal Inkjet: Meeting the Applications Challenge. *International Conference on Digital Printing Technologies* 27–30 (1998).